Science Bulletin 71 (2026) 3617–3623

Contents lists available at ScienceDirect

Science Bulletin

journal homepage: www.elsevier.com/locate/scib

Article

Ultra-small mode volume polariton condensation via precision He^+ implantation

Yannis C. Balas [a,*], Xiaoqing Zhou [a], Evgeniia Cherotchenko [b], Ivan Kuznetsov [c], Sai Kiran Rajendran [d], Giannis G. Paschos [a], Artur V. Trifonov [e], Anton Nalitov [c,f], Hamid Ohadi [d], Pavlos G. Savvidis [a,g,*]

[a] Department of Physics, School of Science, Westlake University, Hangzhou 310014, China
[b] Ioffe Institute, St. Petersburg 194021, Russia
[c] Moscow Institute of Physics and Technology, Dolgoprudnyi 141701, Russia
[d] SUPA, School of Physics and Astronomy, University of St Andrews, St Andrews KY16 9SS, UK
[e] Spin Optics Laboratory, St. Petersburg State University, St. Petersburg 198504, Russia
[f] Russian Quantum Center, Moscow 121205, Russia
[g] Institute of Electronic Structure and Laser and Center for Quantum Science and Technologies FORTH, Heraklion 70013, Greece

A R T I C L E I N F O

Article history:
Received 12 February 2026
Received in revised form 24 April 2026
Accepted 26 May 2026
Available online 11 June 2026

Keywords:
Ion implantation
Polaritonic condensates
Confinement
Focused ion beam
Microcavity

A B S T R A C T

We present a novel method for generating potential landscapes in GaAs microcavities through focused He^+ implantation. The ion beam imprints micron-scale patterns of non-radiative centers that deplete the exciton reservoir and form a loss-defined potential minimum. Under non-resonant pumping, the resulting traps have a lateral size $\leqslant 1.2$ µm and a three-dimensional mode volume of only ≈ 0.6 µm^3, small enough to support a single polariton condensate mode. The implantation process maintains strong coupling and provides lithographic (< 300 nm) resolution. These loss-engineered traps effectively overcome the micrometer-scale limitations of conventional microcavity patterning techniques, opening new avenues for device development and polariton research within the sub-µm regime.

1. Introduction

Exciton-polaritons are quasiparticles formed from the strong coupling of photons and excitons in microcavities. As light-matter quasiparticles, they possess an ultrasmall effective mass, enabling condensation even at room temperature, while also exhibiting significant polariton-matter interactions [1]. Tailoring the in-plane potential of the microcavity (MC) is the workhorse of polaritonic studies [2]. This approach facilitates the exploration of phenomena such as non-equilibrium quantum fluids [3], topological photonics [4], ultrafast optoelectronics [5], and low-dimensional quantum phenomena [6–10]. A broad set of techniques is now employed to shape microcavity potentials, advancing both fundamental research and practical device development.

Taking advantage of the fact that polariton condensates are realized in semiconductor microcavities, the most established methods for achieving tight confinement are provided by semiconductor micro- and nanofabrication techniques. Etched GaAs/AlGaAs micropillars exhibit lasing at diameters as small as 1 µm, reaching single-mode volumes near 10 µm^3 [11]. Open-access microcavities confine polaritons without the need for etching and allow for *in situ* tuning of the Rabi splitting [12]. Photonic crystal defect cavities and bound-state-in-continuum lattices have further enhanced confinement to the wavelength scale, producing room-temperature condensates [13]. Because the interaction-induced blueshift scales inversely with mode volume, shrinking the mode volume enhances polariton-polariton nonlinearities in the few-particle regime, where phenomena such as polariton blockade are predicted [14]. Although these approaches have reduced condensate sizes to a few microns, fabrication disorder in etched pillars, and intrinsic absorption continue to limit coherence, quality factor, and scalability.

Formation and dynamics of polariton condensates generated by spatially profiled optical pumping can be described in terms of effective non-Hermitian potentials [15–18]. Optically imprinted annular potentials have produced trapped condensates that are spatially separated from the excitonic reservoir [19]. Rotating superfluids and deterministic vortex clusters [20], as well as, most recently, vortex "qubit" analogues [21]. However, the diffusion of the long-lived exciton reservoir blurs these additive potentials over several microns, setting a resolution limit.

* Corresponding authors.
E-mail addresses: i.balas@westlake.edu.cn (Y.C. Balas), p.savvidis@westlake.edu.cn (P.G. Savvidis).

https://doi.org/10.1016/j.scib.2026.06.026
2095-9273/

Focused ion beam implantation provides an alternative route that combines precision and repeatability with the relative ease of potential imprinting. The well-developed proton implantation technique is used to form the current aperture [22] and photonic crystal structures [23] in GaAs and GaN VCSELs [24,25]. Sub-micron He^+ stripes in GaAs quantum wells introduce controlled non-radiative broadening while preserving the integrity of cavity optics [26]. High-energy proton irradiation can independently tune exciton and photon energies by intermixing the quantum wells and the distributed Bragg reflector (DBR) layers near the interfaces [27] leading to polariton condensates with tunnable energy.

Here, we demonstrate He^+ implanted traps with lateral dimensions of $\leqslant 1.2$ μm and mode volumes (extracted semi-analytically via the transfer matrix method) of $V_m = L_{\text{eff}}A = 0.65 \pm 0.10$ μm^3, where L_{eff} is the longitudinal cavity length, and A is the cross-sectional area. Furthermore, the tight lateral confinement dictates a quantized energy spacing that is significantly larger than the shallow ~ 1 meV depth of the potential well. Consequently, higher-order modes lie above the potential barrier and cannot be spatially bound, forcing the trap to operate strictly in the single-mode regime. The result is a single-mode condensate with fewer than 200 polaritons. The implantation process locally accelerates non-radiative decay while maintaining strong coupling. The non-radiative centers drain the exciton reservoir, thereby reducing the repulsive blueshift potential while keeping polariton lifetimes unaffected. Under pumping, the depleted reservoir forms a trapping potential. This potential is static and independent of polariton density. These traps feature excellent uniformity and a resolution that surpasses the limitations of both lithographic and optically written patterns. This platform facilitates the implementation of complex design patterns that incorporate even gradient potentials with sub-μm precision, opening a path toward tightly confined, scalable polariton devices and high resolution trap architectures.

2. Materials and methods

2.1. He^+ ion implantation

A 35 keV Focused He^+ ion beams is utilized to irradiate the half-microcavity samples at doses ranging from 1×10^{11} to 1×10^{12} ions/cm^2. This process introduces defects into the crystal lattice, primarily vacancies (indicated by black dots in Fig. 1a) with smaller densities of interstitial and substitutional defects, which are marked with blue in Fig. 1a. TRIM ion scattering simulations [28] indicate that approximately 180 vacancies are generated per implanted ion. In this low-dose regime, defects act only on the optical response of the quantum wells (QWs), leaving the cavity Q intact [29,30]. To maintain a high depth-to-lateral aspect ratio of the ion implantation density, we resort to near-surface implantation of a microcavity structure without the top dielectric DBR (hereafter referred to as "half-microcavity"), followed by top-mirror deposition post-implantation (Fig. 1b).

The sample under investigation consists of a half GaAs/AlGaAs-based semiconductor heterostructure grown by molecular beam epitaxy (MBE), and a top dielectric distributed Bragg reflector (DBR) fabricated through electron beam evaporation. Four sets of three 12 nm GaAs/AlGaAs QWs are embedded between 35 pairs of AlGaAs/AlAs bottom DBR and a top dielectric DBR consisting of 10.5 pairs of Ta_2O_5/SiO_2. The Q-factor of the complete microcavity is estimated using the transfer matrix method (TMM) to be in the order of $Q = 11,000$ (Fig. 1b).

Simulations of the experimental conditions used for ion implantation reveal good overlap between the peak defect density and the depth of the first set of QWs, located 220-270 nm below the surface (Fig. 1b). The lateral defect span at this depth is approximately

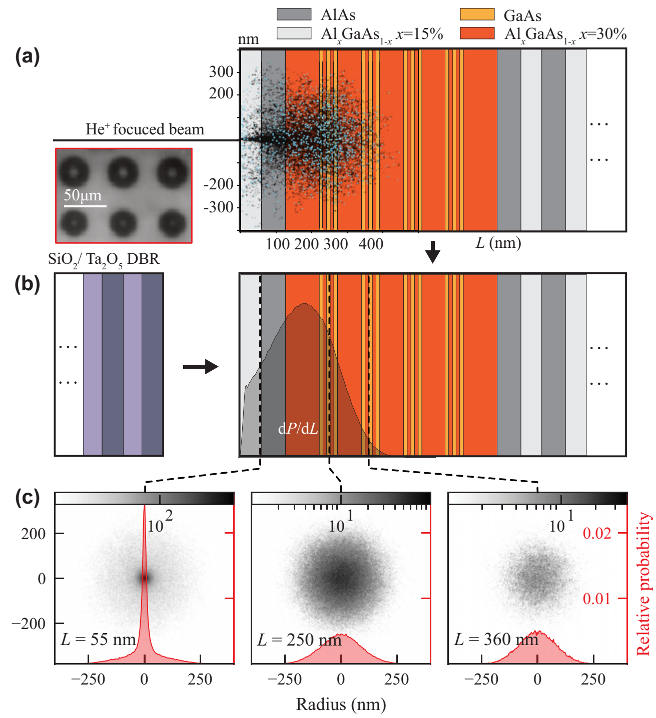

Fig. 1. Schematic representation of sample fabrication steps. (a) Step one: simulated diffusion of vacancies (black dots) caused by He^+ ion implantation (blue dots). The insert in red frame is a PL image of the sample without the top DBR; the dark (black) regions were implanted. (b) Post implantation deposition of top dielectric DBR. Shaded area: relative density of structural defect versus sample depth. (c) Lateral diffusion profiles for different depth zones of 50 nm; Central depths denoted in each frame.

300 nm (Fig. 1c, middle). The current implantation technique allows for < 50 nm structural resolution for QWs located near the surface (Fig. 1c, left).

2.2. QW optical characterization

The effect of He^+ implantation induced defects on the QWs are limited to non-radiative broadening while (in this dose range) leaving the radiative decay rate intact [26]. Non-radiative broadening is evident by photoluminescence (PL), time-resolved PL (TRPL), and reflectivity measurements independently. All measurements in this section are performed at 4 K on the "half-microcavity" sample.

Micro-reflectivity spectra are obtained using a broadband white-light source, which is directed onto the sample through a microscope objective. Implantation-induced vacancies create non-radiative recombination centers, reducing resonant excitonic absorption as the implantation dose increases (Fig. 2a).

For the PL emission study, a continuous-wave Ti:Sapphire laser is used to optically pump the sample non-resonantly at 1.710 eV with ≈ 1 μm spot while emitted PL is collected through a microscope objective. A long-pass filter cuts off the reflection of the pump laser. The PL intensity decreases with increasing helium ion doses due to the enhancement of non-radiative pathways, which reduces the quantum efficiency of the QWs (Fig. 2b).

For TRPL experiments, we utilize a mode-locked 150 fs pulse Ti: Sapphire laser, and PL decay dynamics is measured using a streak camera across a range of implantation doses. We observe a clear reduction in PL lifetime (τ) with increasing ion doses (Fig. 2c), a clear signature of enhanced non-radiative recombination rates.

Several conclusions can be drawn from these measurements based on the rate equation, governing the dynamics of exciton density N:

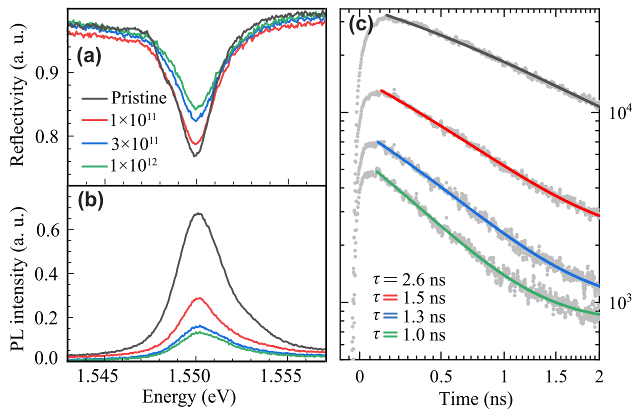

Fig. 2. Optical effect of He^+ ion implantation in GaAs quantum wells: (a) PL quenching, (b) reduction of resonant QW absorption, and (c) reduction of PL emission lifetime on various ion implantation doses in QWs.

$$\frac{dN}{dt} = P - (\gamma_R + \gamma_{NR})N, \quad (1)$$

where P is the pump term and γ_R (γ_{NR}) are the radiative (non-radiative) rates. Implantation increases γ_{NR}, which (i) lowers the steady-state exciton density $N = P/(\gamma_R + \gamma_{NR})$ and therefore the blueshift potential and (ii) reduces the PL yield $I = N\gamma_R$ without noticeably altering γ_R [26]. The resulting spatial modulation of N (high outside, strongly depleted inside the implanted area) acts as an effective non-Hermitian potential, a mechanism we exploit in the confinement experiments that follow. Crucially, the confinement mechanism in our traps is overwhelmingly dominated by this targeted reduction of the excitonic lifetime rather than structural deformation. He^+ ion implantation at these energies creates highly localized non-radiative point defects without introducing massive lattice strain. Consequently, local refractive index variations and strain-induced band shifts are negligible $\Delta n \leqslant 1\%$ [30] (as confirmed by the PL and reflectivity spectra in Fig. 2a and b), and the confining potential landscape is generated purely by the spatial shaping of the repulsive steady-state exciton reservoir.

3. Results and discussion

3.1. Polariton condensate confinement

We continue our investigation on the full DBR-capped microcavity. First, we verified that strong coupling is preserved in the implanted areas using angle-resolved micro-photoluminescence at 4 K. Under low non-resonant pump power (well below the nonlinear response), the spectra reveal both the lower and upper-polariton branches, displaying the clear anticrossing characteristic of the strong coupling regime. By tracking the peak positions of the two branches, we extracted the mode separation $\Delta E(k_\parallel) = E_{UP} - E_{LP}$. The minimum of $\Delta E(k_\parallel)$ yields a Rabi splitting of 8.55 ± 0.11 meV. The uncertainty stems from the experimental spectral resolution of 0.04nm while the measured value remains constant across all regions: pristine, low (1×10^{11} cm^{-2}), medium (3×10^{11} cm^{-2}), and high dose (1×10^{12} cm^{-2}) as shown in Fig. 3. Next, to evaluate the effect of implantation on the polariton linewidth, we extracted the full-width at half-maximum (FWHM) of the lower polariton branch at $k_\parallel = 0$. We observe a substantial narrowing of the linewidth upon the introduction of defects, dropping by 113 μeV from 0.438 to 0.325 meV (pristine to low dose). This is attributed to the severe depletion of the localized exciton reservoir, which strongly suppresses polariton-reservoir dephasing. Notably, while higher doses show a slight subsequent broadening of 0.342 to 0.367 meV (that is below our spectral resolution limit that corresponds to 0.077 meV), the linewidth of the implanted regions remain strictly narrower than that of the pristine sample.

These results demonstrate that ion implantation in this dose range does not degrade the excitonic oscillator strength or the collective light-matter coupling. The ion-induced defects only affect the non-radiative exciton loss rate [26,31,32]. Consequently, we observe condensation in both pristine and uniformly implanted regions, though the respective condensation threshold powers significantly increase with higher implantation doses due to the defect-induced non-radiative losses (details in Supplementary Material S1).

Subsequently, we observed trapped polariton condensation in a small implanted dot region of 1.2 μm diameter (Fig. 4a and b (left)), pumped by a wide excitation spot of 40 μm to ensure homogeneous, flat, and standardized (across all configurations that follow) illumination, while minimizing ballistic losses [33]: since the blueshift potential depends on the exciton density, the implanted dot effectively forms a potential well due to locally enhanced excitonic losses. At the same time, polariton losses are mainly governed by the rate of photon escape from the cavity, which is limited by its Q-factor. Both DBRs and the optical cavity-and thus the polariton lifetime-remain uniform and virtually unaffected by the ion implantation. Polaritons condensed within the implanted dot exhibit a clear spatial confinement (Fig. 4b (left) insets). Notably, while uniformly implanted, unconfined regions (Fig. 3 and Fig. S1 online) exhibit an increased condensation threshold due to defect-induced losses, the trapping configurations (as in our 1.2 μm implanted dot) heavily suppress ballistic radial losses [19,33], lowering the condensation threshold (Fig. 4b (right)) compared to pristine region excitation (Fig. 4a (right)).

Although the resolution of ion-induced defect patterning is in the submicron range, the trapping potential resolution is affected by the exciton in-plane diffusion length $L_X = \sqrt{D_X \tau_X}$, where D_X is the exciton diffusion coefficient and τ_X is the reservoir exciton lifetime [34]. The diffusion coefficient, in turn, depends on the momentum-relaxation time τ_m through $D_X \simeq (k_B T/M_X)\tau_m$ (with $M_X = m_e + m_h$ the exciton mass), and τ_m scales with the defect density as $\tau_m \simeq [N_i \sigma_{eff} v_{th}]^{-1}$, where N_i is the defect density, σ_{eff} the effective scattering cross-section, and $v_{th} = \sqrt{2k_B T/M_X}$ the thermal velocity. Comparing the SRIM-estimated vacancy density at the QW plane ($\sim 7 \times 10^{18}$ cm^{-3} at the highest dose) with typical pristine GaAs QW defect densities ($\sim 10^{16}$ cm^{-3} [35]), one expects a three-order-of-magnitude reduction of τ_m and therefore of D_X in the implanted region. In combination with the measured threefold reduction of the reservoir lifetime τ_x (Fig. 2c), this yields submicron diffusion length L_X in the implanted areas and trapping potential resolution.

Our trapping scheme highlights the effectiveness of engineered defect loss landscapes in reducing exciton density, offering a novel pathway for achieving efficient polariton confinement and condensation. This tight confinement leads to a reduction in the steady-state number of polaritons N. Specifically, $N_{tr} \approx 150$ while $N_{pr} \approx 1300$, where N_{tr} corresponds to the trapped condensate shown in Fig. 4b, and N_{pr} corresponds to the pristine sample condensation at $P = 1.6P_{th}$. For details regarding the polariton number calculation see Supplementary Material S2.

3.2. Wire traps

The universality of the trapping technique is tested with patterning microwires of various widths and with length of 45 μm (Fig. 5a), demonstrating confinement effects analogous to those observed in a quasi-1D quantum well (QW). Real space imaging

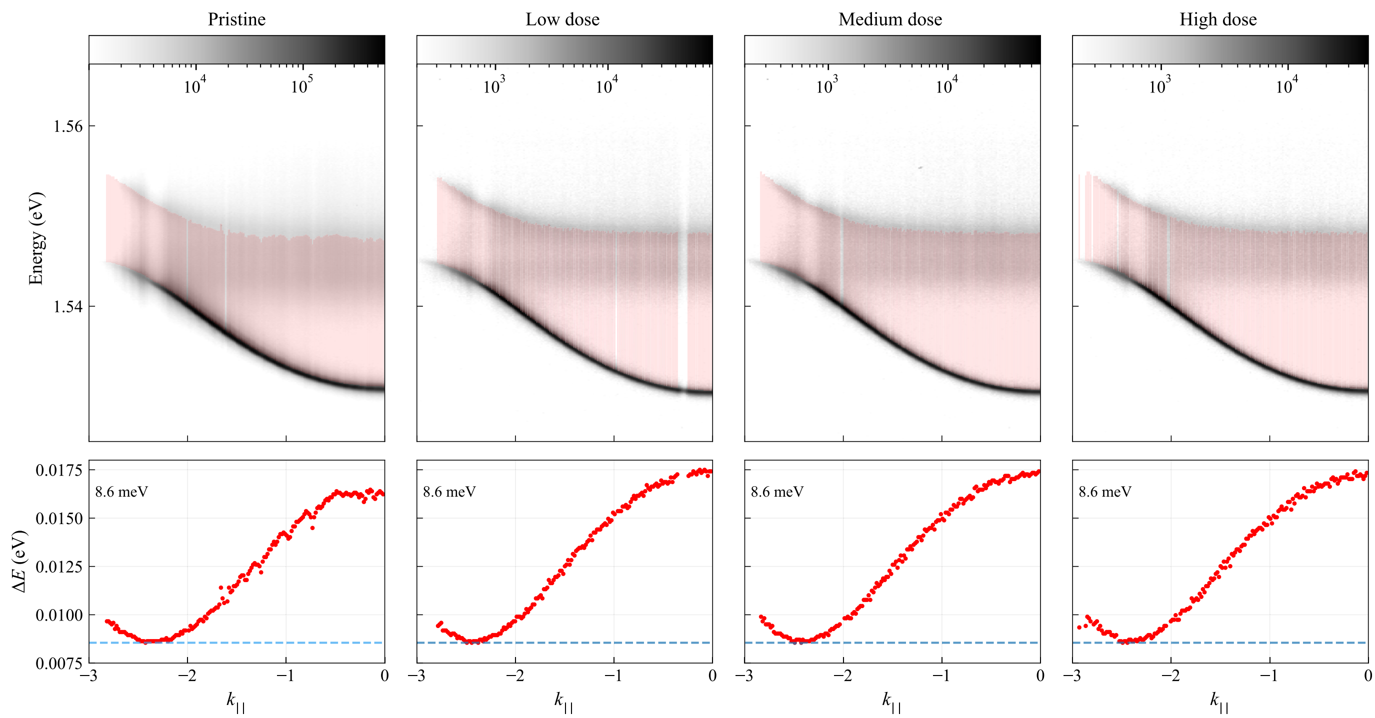

Fig. 3. Analysis of the Rabi splitting measurement for the pristine and implanted regions. The upper panels show the measured angle-resolved photoluminescence dispersions (logarithmic color maps). The red shaded areas correspond to the areas between UP and LP branches traced with a peak finding algorithm. The lower panels present the corresponding energy separation $\Delta E(k_{\parallel}) = E_{UP} - E_{LP}$ extracted directly from the experimental spectra. The minima of $\Delta E(k_{\parallel})$ define the apparent Rabi splitting at zero detuning for each implantation dose denoted with blue dashed lines.

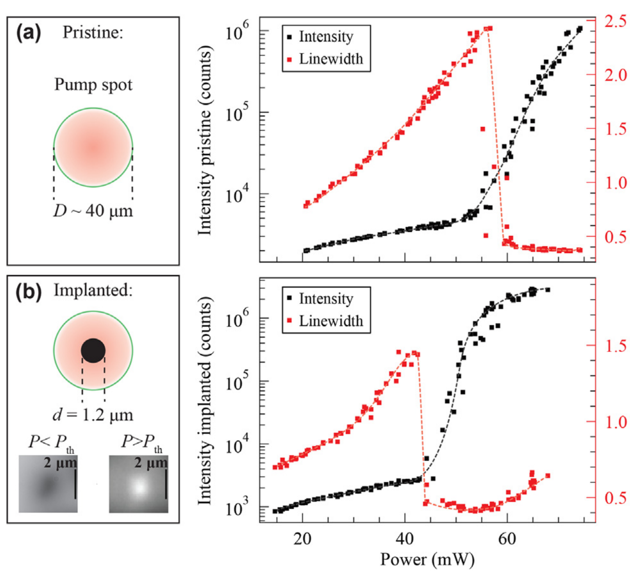

Fig. 4. Confinement in implanted dot. Measured power dependence (pump power vs emitted PL intensity) from a pristine region of the sample (a), and from an area of the sample with a $d = 1.2$ µm implanted dot (b). Experimental data of real space PL intensity below and above condensation threshold (insets in (b)): for $P < P_{th}$ PL emission mostly comes from pristine sample while for $P > P_{th}$ most of the intensity comes from the implanted region. Both measurements were performed using a $D \approx 40$ µm laser spot. Dashed lines act as guide for the eye.

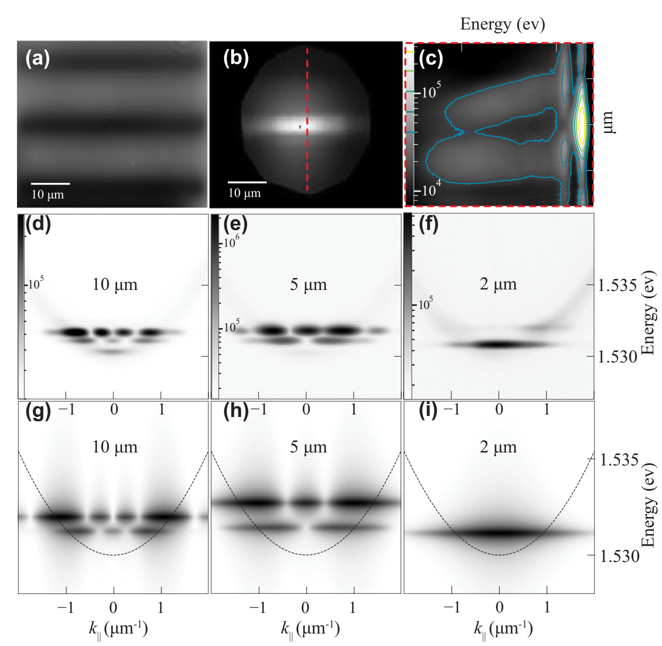

Fig. 5. Wire traps. Top row (experimental data): real space image of a region implanted with $W = 5$ µm wires (dark regions) under the condensation threshold (a), above condensation threshold (b). (c) is the spectral analysis of the cross-section indicated by a red dashed line in (b). Middle row (experimental data): far-field spectroscopy above the condensation threshold of wires with widths (d) $W = 10$ µm, (e) $W = 5$ µm, (f) $W = 2$ µm. Measurements were performed using a $D \approx 40$ µm laser spot. Bottom row: analytical calculation (g, h, i) of (d, e, f) respectively. Parameters: $l_0 = 3$ µm, $\varepsilon = 2.5, n_0 = 7.5, c = 0.1$.

revealed bright emission from the center of the wire for $P > P_{th}$ under the standard $D \approx 40\upsilon$ broad excitation, the condensate emission tapers off naturally before reaching the physical structural edges because the local optical gain smoothly drops below the condensation threshold (Fig. 5b). An energy-resolved vertical slice taken from the center of Fig. 5b reveals that the emission from the edges of the implanted wire exhibits suppressed intensity and higher energy compared to the center of the trap, which emits brightly at lower energy (Fig. 5c). Angle-resolved emission indicates that the energy levels depend on wire width (Fig. 5d–f), consistent with theoretical predictions for 1D potential wells (Fig. 5g–i).

We describe the polariton condensates in quasi-1D wires near the condensation threshold, neglecting nonlinearities, with the non-Hermitian variation of 1D Schroedinger equation:

$$\left[-\frac{\hbar^2}{2m}\partial_x^2+\frac{\alpha+i\beta}{2}N(x)-i\frac{\hbar\Gamma}{2}-i\hbar\partial_t\right]\Psi(x,t)=0, \tag{2}$$

where m is the effective polariton mass, $N(x)$ is the spatially profiled exciton reservoir density, α and β are the parameters governing the strength of conservative and dissipative parts of interaction with the reservoir, and Γ is the polariton radiative loss rate.

The sub-micron spatial resolution of the ion implantation technique combined with suppressed exciton diffusion in the implanted region allows us to assume a sharp reservoir density profile: $N(x)=cN_0$ if $|x|<D/2$ and N_0 if $|x|>D/2$, with D the wire width. Here $c<1$ is the ratio of steady-state reservoir exciton densities, governed by the ratio of loss rates in the implanted and pristine regions. The linear spectral properties of the Eq. (2) are then obtained by solving the non-Hermitian extension of the QW problem.

We introduce the characteristic time $t_0=2/\Gamma$ and the characteristic attenuation length $l_0=\sqrt{\hbar/(2m\Gamma)}$ to obtain the dimensionless stationary form of Eq. (2):

$$\tilde{\omega}\Psi=\left[-\partial_\chi^2+(\varepsilon+i)n-i\right]\Psi, \tag{3}$$

with normalized coordinate $\chi=x/l_0$, the ratio of Hermitian and anti-Hermitian potential parts $\varepsilon=\alpha/\beta$, normalized reservoir density $n=2\beta N/(\hbar\Gamma)$ and complex energy $\tilde{\omega}$.

In full analogy with the conservative problem, the effective Hamiltonian symmetry allows even and odd eigenstates $\Psi(\chi)=\pm\Psi(-\chi)$. Outside the implanted region ($|\chi|>d/2$) with $d=D/l_0$, where the reservoir density takes the value $n_0=2\beta N_0(\hbar\Gamma)$ representing the steady-state exciton reservoir density, it is convenient to denote the solution vanishing at $|\chi|\to\infty$ as $B\exp[-\varkappa(\chi-d/2)]$ for $\chi>d/2$ and $\pm B\exp[\varkappa(\chi-d/2)]$ for even and odd states at $\chi<-d/2$. Here $\varkappa=\sqrt{(\varepsilon+i)n_0-i-\tilde{\omega}}$ and the principal branch $\mathrm{Re}\{\varkappa\}>0$ is selected to avoid divergence at $|\chi|\to\infty$. Notably, such evanescent solutions simultaneously satisfy the boundary conditions for polariton currents $J(\chi)=\hbar\mathrm{Im}\{\Psi^*\partial_\chi\Psi\}/m$, namely, $J(\chi>d/2)>0$ and $J(\chi<-d/2)<0$. In the implanted region, the reservoir density is reduced by a factor $c<1$, producing an effective potential $(\varepsilon+i)cn_0$. The corresponding even and odd wave functions read $\Psi=A\cos(q\chi)$ and $\Psi=A\sin(q\chi)$, respectively, where $q=\sqrt{\tilde{\omega}+i-(\varepsilon+i)cn_0}$ with the selection of the principal square root branch $\mathrm{Re}\{q\}>0$.

The eigenstates are obtained by matching the piecewise-defined wave functions at $|\chi|=d/2$, or equating $\tan(qd/2)$ to $\varkappa/q$ for even states and to $-q/\varkappa$ for odd states. Solving for $\tilde{\omega}$ on the complex plane yields the spectrum of discrete trapped polariton modes $\tilde{\omega}_j$ along with the corresponding wave functions $\Psi_j(x)$. While the emission energy of a polariton mode is given by the real part of its energy $\omega_j=\mathrm{Re}\{\tilde{\omega}_j\}\in[c\varepsilon n_0,\varepsilon n_0]$, the imaginary part $g_j=\mathrm{Im}\{\tilde{\omega}_j\}\in[-1+cn_0,-1+n_0]$ describes its growth rate and thus the stationary population under cw pumping, provided $g_j>0$.

The reciprocal space emission profiles $|\tilde{\Psi}_j(k)|^2$ of the trapped polariton modes can be analytically expressed in the energies $\tilde{\omega}_j$ by calculating the Fourier transform of $\Psi_j(x)$, see Supplementary Material S3. The total multimode emission profile along the direction, perpendicular to the microwire, is given by the sum of all contributions over all trapped modes, characterized with stationary populations $g_j>0$ and unitary broadening, given by the Lorentzian factor:

$$I(k,\omega)=\sum_j\frac{g_j|\tilde{\Psi}_j(k)|^2}{1+(\omega-\omega_j)^2}. \tag{4}$$

3.3. Ring traps

In ring-shaped traps with outer diameters of $D=35$ μm and inner diameters of $d=4$ μm (Fig. 6a), the excitation beam generates a radial potential profile. The unimplanted center and outer rim accumulate a high exciton density under the excitation beam, resulting in elevated blueshift potential. The implanted area, characterized by reduced exciton density, forms an annular potential well. Polaritons condense within this well, exhibiting radially symmetric modes (Fig. 6b). Angle-resolved emission confirms the presence of discrete energy levels associated with this confinement (Fig. 6c).

Similarly to the case of microwires, non-Hermitian polariton confinement in isotropic ring-shaped traps is described by the equation

$$\left[-\frac{\hbar^2}{2m}\Delta_{r,\varphi}+\frac{\alpha+i\beta}{2}N(r)-i\frac{\hbar\Gamma}{2}-i\hbar\partial_t\right]\Psi(r,\varphi,t)=0, \tag{5}$$

with $\Delta_{r,\varphi}$ being the Laplacian expressed in polar coordinates. Sharp-edge annular traps correspond to a piecewise-defined reservoir density (depicted as a binary loss mask in Fig. 6d): $N(r)=N_0$ if $r<d/2$ or $r>D/2, N(r)=cN_0$ if $d/2<r<D/2$.

The dimensionless stationary variant of Eq. (5) reads

$$\left[-\frac{1}{\rho}\frac{\partial}{\partial\rho}\left(\rho\frac{\partial}{\partial\rho}\right)-\frac{1}{\rho^2}\frac{\partial^2}{\partial\varphi^2}+(\varepsilon+i)n-i-\tilde{\omega}\right]\Psi(\rho,\varphi), \tag{6}$$

with the normalized distance from the trap center $\rho=r/l_0$.

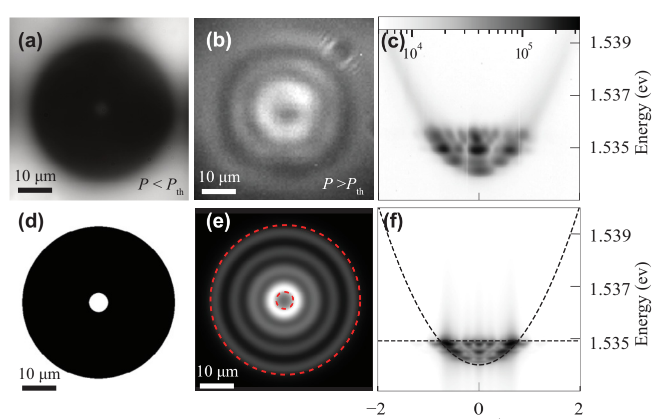

Fig. 6. Ring traps. Top row (experimental data): (a) real space image of PL emission below threshold ($P<P_{\rm th}$): the implanted region appears dark. (b) Above threshold ($P>P_{\rm th}$): a bright set of concentric rings appears inside the implanted annulus, evidencing quantised radial modes of the condensate. (c) Angle-resolved emission at ($P>P_{\rm th}$) (logarithmic colour scale) showing discreet energy states. Measurements were performed using a $D\approx40$ μm laser spot. Bottom row (calculations): (d) binary loss mask used in the numerical model (black = high loss). (e) Steady-state condensate density obtained from the non-Hermitian Schrödinger solutions are in agreement with experimental results; the red dashed circle marks the implanted rim. (f) Simulated k-space spectrum of confined modes. The dashed curve represents the un-confined polariton lower polariton branch. Resulting potential depth marked with a dashed horizontal line. Parameters: $l_0=5$ μm, $\varepsilon=5, n_0=4.5, c=0.25$.

The radial symmetry of the effective potential, stemming from the reservoir, and the boundary conditions at $r = 0$ and $r \to \infty$ govern the form of the wave function $\Psi_l(r,\varphi) = \Phi_l(\varphi)R_l(r)$:

$$\Psi_l(\rho,\varphi) = \exp(il\varphi) \times \begin{cases} AI_l(\varkappa\rho), & \rho < \rho_1, \\ BJ_l(q\rho) + CY_l(q\rho), & \rho_1 < \rho < \rho_2, \\ DK_l(\varkappa\rho), & \rho > \rho_2 \end{cases} \quad (7)$$

where A, B, C, D are complex coefficients related with the normalization condition $2\pi\int|\Psi(r,\varphi)|^2 r\mathrm{d}r = 1$.

Matching the wave function values and spatial derivatives at $\rho_1 = R_1/l_0$ and $\rho_2 = R_2/l_0$ yields the transcendental complex equation for complex energies $\tilde{\omega}_{l,j}$ of the effectively trapped polariton states, labeled with integer angular and radial numbers l and j. The analytical expressions for the Fourier transforms of the wave functions $\tilde{\Psi}_{l,j}(k,\varphi_k)$ is given in Supplementary Material S3. Due to the radial trap symmetry, the emission spectrum $I(k,\omega)$ is isotropic and is determined by the same expression as in Eq. (4), but with summation carried out over all integer l and j, corresponding to macroscopically populated polariton modes $g_{l,j} = \mathrm{Im}\{\tilde{\omega}_{l,j}\} > 0$, emitting at frequencies $\omega_{l,j} = \mathrm{Re}\{\tilde{\omega}_{l,j}\}$ producing the steady-state condensate density shown in Fig. 6e. Notably, emission from excited trapped polariton modes at higher frequencies $\omega < \varepsilon n_0$ is stronger compared to that from the ground state (see simulated spectrum in Fig. 6f) in full agreement with the experimentally measured spectra in Fig. 5d, e and Fig. 6c. This vividly demonstrates that the observed polariton condensates are strongly out-of-equilibrium and thus confirms the validity of our non-Hermitian description.

4. Conclusion

Focused He^{+} ion implantation provides a robust technique for engineering lateral confinement in polariton microcavities. By tailoring the patterns we achieved high-precision control over the effective non-Hermitian trapping potentials generating polaritons condensates in dots, microwires and ring-shaped traps. Notably, the conservative and dissipative contributions to these potentials are comparable, which makes our system a suitable platform for implementation and study of non-Hermitian Hamiltonians. Moreover, extreme spatial resolution of the effective complex potentials allows conveniently describing trapped polariton condensates with the non-Hermitian extension of conservative textbook quantum–mechanical models used in semiconductor heterostructures. These findings emphasize the role of excitonic loss landscapes in the design of efficient polariton traps and highlight the potential of this technique for scalable sub-μm polaritonic applications.

Conflict of interest

The authors declare that they have no conflict of interest.

Acknowledgments

Pavlos G. Savvidis acknowledges support by the Innovation Program for Quantum Science and Technology (2023ZD0300300), the Innovation Resource Allocation of Westlake University-Zhejiang Provincial Natural Science Foundation of China under Grant No. XHD24A2401, and the Westlake University project No. 102510036022301. Anton Nalitov acknowledges support by the Russian Science Foundation under Grant No. 25–12-00135. Sai Kiran Rajendran and Hamid Ohadi acknowledge support from the Leverhulme Trust through Grant No. RPG-2022–188. Artur V. Trifonov acknowledges Saint Petersburg State University (Grant No. 125022803069–4). The authors acknowledge the SPbU Resource Center ‘Nanotechnology’ for the helium implantation. This work was supported by the Hellenic Founndation for Research and Innovation (H.F.R.I.) through the QuComPol project (Project No. 25442), We acknowledge E. Mavrotsoupakis for his contribution to the initial spectroscopic characterization of the samples.

Author contributions

Pavlos G. Savvidis, Yannis C. Balas, and Artur V. Trifonov conceived the project. Yannis C. Balas led the investigation, analysis, and simulations. Xiaoqing Zhou and Artur V. Trifonov contributed to the implantation, investigation, and simulations. Evgeniia Cherotchenko, Ivan Kuznetsov, and Anton Nalitov performed the theoretical modeling. Sai Kiran Rajendran and Giannis G. Paschos carried out the modeling, and DBR fabrication. Yannis C. Balas, Anton Nalitov, Hamid Ohadi, and Pavlos G. Savvidis wrote the manuscript. Pavlos G. Savvidis supervised the project.

Appendix A. Supplementary material

Supplementary data to this article can be found online at https://doi.org/10.1016/j.scib.2026.06.026.

References

[1] Kasprzak J, Richard M, Kundermann S, et al. Bose-Einstein condensation of exciton polaritons. Nature 2006;443:409–14.
[2] Schneider C, Winkler K, Fraser MD, et al. Exciton-polariton trapping and potential landscape engineering. Rep Prog Phys 2016;80:016503.
[3] Carusotto I, Ciuti C. Quantum fluids of light. Rev Mod Phys 2013;85:299–366.
[4] Klembt S, Harder TH, Egorov OA, et al. Exciton-polariton topological insulator. Nature 2018;562:552–6.
[5] Ballarini D, De Giorgi M, Cancellieri E, et al. All-optical polariton transistor. Nat Commun 2013;4:1778.
[6] Moreau E, Robert I, Gérard J, et al. Single-mode solid-state single photon source based on isolated quantum dots in pillar microcavities. Appl Phys Lett 2001;79:2865–7.
[7] Santori C, Fattal D, Vučković J, et al. Indistinguishable photons from a single-photon device. Nature 2002;419:594–7.
[8] Heindel T, Schneider C, Lermer M, et al. Electrically driven quantum dot-micropillar single photon source with 34% overall efficiency. Appl Phys Lett 2010;96:011107.
[9] Klaas M, Schlottmann E, Flayac H, et al. Photon-number-resolved measurement of an exciton-polariton condensate. Phys Rev Lett 2018;121:047401.
[10] Bajoni D, Senellart P, Wertz E, et al. Polariton laser using single micropillar GaAs-GaAlAs semiconductor cavities. Phys Rev Lett 2008;100:047401.
[11] Czopak U, Prilmüller M, Schneider C, et al. Polariton lasing in micropillars with one micrometer diameter and position-dependent spectroscopy of polaritonic molecules 2021. ArXiv:2102.04186.
[12] Li F, Li Y, Giriunas L, et al. Condensation of 2D exciton-polaritons in an open-access microcavity. J Appl Phys 2022;131:093101.
[13] Wu X, Zhang S, Song J, et al. Exciton polariton condensation from bound states in the continuum at room temperature. Nat Commun 2024;15:3345.
[14] Verger A, Ciuti C, Carusotto I. Polariton quantum blockade in a photonic dot. Phys Rev B 2006;73:193306.
[15] Gao T, Estrecho E, Bliokh KY, et al. Observation of non-Hermitian degeneracies in a chaotic exciton-polariton billiard. Nature 2015;526:554–8.
[16] Sun Y, Yoon Y, Khan S, et al. Stable switching among high-order modes in polariton condensates. Phys Rev B 2018;97:045303.
[17] Nalitov AV, Sigurdsson H, Morina S, et al. Optically trapped polariton condensates as semiclassical time crystals. Phys Rev A 2019;99:033830.
[18] Cherotchenko ED, Sigurdsson H, Askitopoulos A, et al. Optically controlled polariton condensate molecules. Phys Rev B 2021;103:115309.
[19] Askitopoulos A, Ohadi H, Kavokin AV, et al. Polariton condensation in an optically induced two-dimensional potential. Phys Rev B 2013;88:041308.
[20] Del Valle-Inclan Redondo Y, Schneider C, Klembt S, et al. Optically driven rotation of exciton-polariton condensates. Nano Lett 2023;23:4564–71.
[21] Barrat J, Tzortzakakis AF, Niu M, et al. Qubit analog with polariton superfluid in an annular trap. Sci Adv 2024;10:eado4042.
[22] Ressel P, Strusny H, Gramlich S, et al. Optimised proton implantation step for vertical-cavity surface-emitting lasers. Electron Lett 1993;29:918–9.
[23] Kasten AM, Siriani DF, Hibbs-Brenner MK, et al. Beam properties of visible proton-implanted photonic crystal vessels. IEEE J Sel Top Quantum Electron 2011;17:1648–55.

[24] Leonard J, Cohen D, Yonkee B, et al. Nonpolar iii-nitride vertical-cavity surface-emitting lasers incorporating an ion implanted aperture. Appl Phys Lett 2015;107:011102.
[25] Hamaguchi T, Tanaka M, Nakajima H. A review on the latest progress of visible GaN-based VCSELs with lateral confinement by curved dielectric DBR reflector and boron ion implantation. Jpn J Appl Phys 2019;58:SC0806.
[26] Kapitonov YV, Shapochkin PY, Petrov YV, et al. Effect of irradiation by He^+ and Ga^+ ions on the 2D-exciton susceptibility of InGaAs/GaAs quantum-well structures. Phys Status Solidi B 2015;252:1950–4.
[27] Fraser MD, Tan HH, Redondo YDVI, et al. Independent tuning of exciton and photon energies in an exciton-polariton condensate by proton implantation-induced interdiffusion. Adv Opt Mater 2023;11:2201569.
[28] Ziegler JF, Ziegler M, Biersack J. SRIM-The stopping and range of ions in matter (2010). Nucl Instrum Methods Phys Res B 2010;268:1818–23.
[29] Paxton A, Carson R, Schone H, et al. Damage from proton irradiation of vertical-cavity surface-emitting lasers. IEEE Trans Nucl Sci 1997;44:1893–7.
[30] Wendler E, Wesch W, Götz G. Defects in weakly damaged ion-implanted GaAs and other III-V semiconductors. Phys Status Solidi A 1989;112:289–99.
[31] Savona V, Andreani LC, Schwendimann P, et al. Quantum well excitons in semiconductor microcavities: unified treatment of weak and strong coupling regimes. Solid State Commun 1995;93:733–9.
[32] Houdré R, Stanley RP, Ilegems M. Vacuum-field rabi splitting in the presence of inhomogeneous broadening: resolution of a homogeneous polariton doublet in an inhomogeneously broadened exciton system. Phys Rev Lett 1994;73:2043–6.
[33] Utesov OI, Park M, Choi D, et al. Universal condensation threshold dependence on pump beam size for exciton-polaritons. Commun Phys 2025;8:8286.
[34] Schram PPJM. Kinetic Theory of Gases and Plasmas. Netherlands: Springer; 1991.
[35] Shafi M, Mari RH, Khatab A, et al. Deep-level transient spectroscopy of GaAs/AlGaAs multi-quantum wells grown on (100) and (311)B GaAs substrates. Nanoscale Res Lett 2010;5:1948–51.